

Experimental demonstration of plasmon-soliton waves

Tintu Kuriakose¹, Gilles Renversez^{2,*}, Virginie Nazabal^{3,5}, Mahmoud M. R. Elsawy²,
Nathalie Coulon⁴, Petr Němec⁵, and Mathieu Chauvet^{1,*}

June 3, 2021

¹ FEMTO-ST Institute, CNRS, University of Bourgogne Franche-Comté, 15B avenue des Montboucons, 25030 Besançon, France

² Aix-Marseille Univ, CNRS, Centrale Marseille, Institut Fresnel, 13013 Marseille, France

³ Univ Rennes, CNRS, ISCR (Institut des Sciences Chimiques de Rennes) – UMR 6226, 35000 Rennes, France

⁴ Univ Rennes, CNRS, IETR (Institut d'Electronique et de Télécommunications de Rennes) – UMR 6164, 35000 Rennes, France

⁵ Department of Graphic Arts and Photophysics, Faculty of chemical Technology, University of Pardubice, Studentská 573, 53210 Pardubice, Czech Republic

*mathieu.chauvet@univ-fcomte.fr and gilles.renversez@univ-amu.fr

Abstract

Controlling low power light beam self-confinement with ultrafast response time opens up opportunities for the development of signal processing in microdevices. The combination of highly nonlinear medium with the tight confinement of plasmonic waves offers a viable but challenging configuration to reach this goal. Here, we report the experimental observation of plasmon-soliton waves propagating in a chalcogenide-based four-layer planar geometry engineered to limit plasmon propagation losses while exhibiting efficient Kerr self-focusing at moderate power. The observations reveal a strongly enhanced self-focusing undergone by a self-trapped beam propagating inside the structure. As expected from theory, only TM polarized waves exhibit such a behaviour. Different experimental arrangements are tested that unambiguously reveal the nonlinear plasmon-soliton waves which are corroborated by simulations.

The efficiency of nonlinear optical processes is well known to benefit from extreme light confinement. One way to achieve such a strong electromagnetic field is to exploit light interactions with metal nanostructures. The surface plasmon polariton (SPP) [1] at a metal-dielectric interface, associated with both a collective oscillation of free charges in the metal and an extremely confined electromagnetic wave, has been a key discovery. Since then, plasmonics has evolved into a flourishing research field [2]. It was then natural to combine the fields of plasmonics and nonlinear optics to exploit these intense optical fields, allowing researchers to envision a variety of fascinating and original physical phenomena with great application potential. In addition to providing enhanced nonlinear effects with ultra-fast response times, plasmonic nanostructures allow nonlinear optical components to be scaled down in size. As a consequence, the field of nonlinear plasmonics [3] has grown significantly in recent years with applications such as frequency conversion [4], switching and modulation [5]. However, this field of research is still in its infancy.

More specifically, first descriptions of one-dimensional nonlinear plasmon-solitons and nonlinear surface waves at metal/dielectric and dielectric/dielectric interfaces were unveiled in the early eighties [6–9]. The concept being to propagate a plasmon-polariton wave at a metal-nonlinear material interface in order to induce an exalted Kerr self-focusing effect giving rise to a self-trapped wave. Up to now, the problem has been tackled only theoretically, based on analytical and numerical calculations [10–20] dealing with both spatial and temporal beam trapping. Despite this constant and comprehensive modelling development, no experimental evidence of self-trapped nonlinear plasmonic waves, named plasmon-solitons in [10], has yet been revealed despite almost four decades since the first publication on nonlinear surface waves [6-7]. Among the practical challenges inherent to this plasmon assisted self-focusing demonstration are the large propagation losses associated with plasmons, the request for a strong Kerr coefficient, and the limitations due to the damage threshold intensity of the plasmonic structure.

In the present work, a four-layer slab component is designed and fabricated to support a SPP with moderate losses along with a strong Kerr nonlinear effect. This structure allows the first experimental observation of a hybrid plasmon-soliton wave that combines a spatial soliton and a SPP in a single wave. It reveals a strong enhancement of the beam two-dimensional self-trapping efficiency due to the plasmonic effect occurring for such type of nonlinear wave. The content of the article is as follows: we start by describing the structure design and fabrication steps. Secondly, nonlinear optical characterizations are presented. Finally, numerical simulations are confronted to the experiments and results are discussed.

Design and fabrication of the structures

The origin of our nonlinear plasmonic component is a planar chalcogenide waveguide that possesses the suitable nonlinear properties to form Kerr spatial solitons at near-infrared wave-

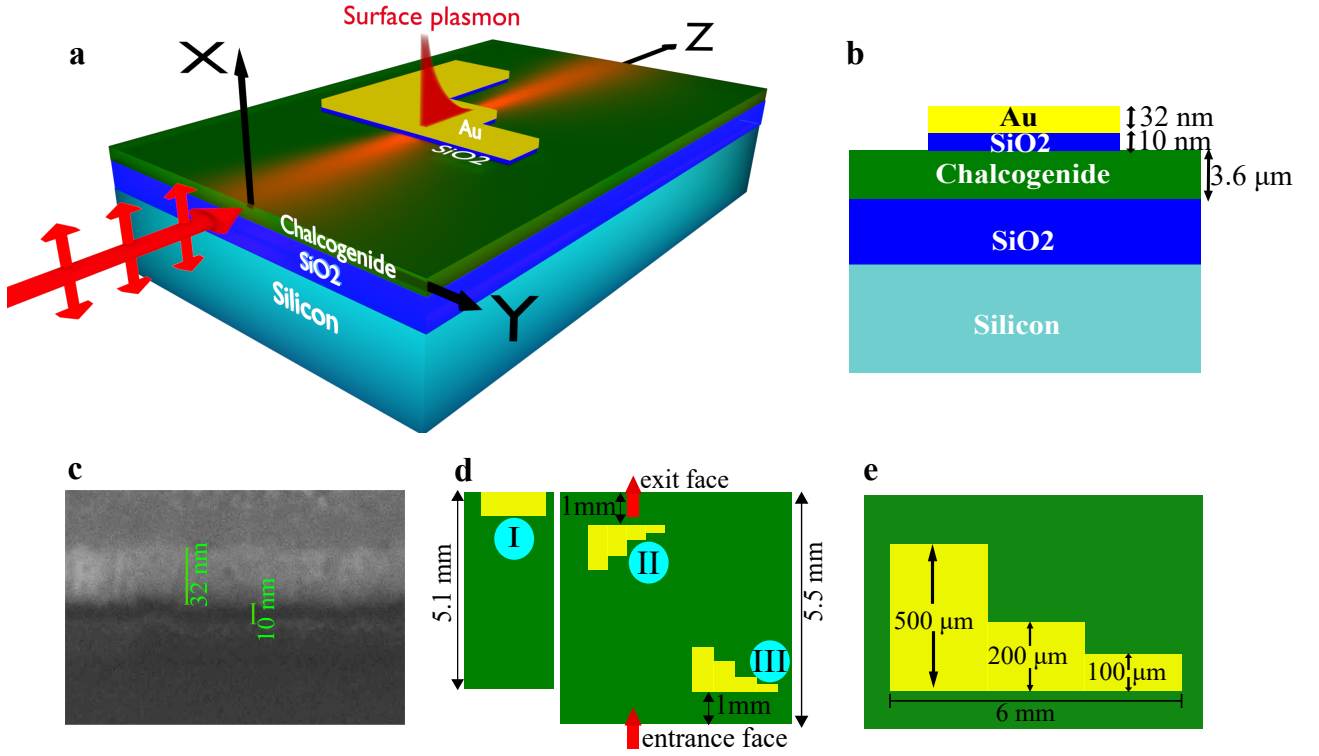


Figure 1: View of the structure. a, artistic 3-D view of the experiment. b, schematic description of the cross section of the sample with the plasmonic structure. c, SEM image of the Au/SiO₂/chalcogenide interfaces. d, schematic overall top view of the sample showing the three studied configurations denoted by I, II and III. e, detailed schematic top view of the used staircase metallic pattern.

lengths, as demonstrated in refs [21,22]. A metal film must be present for the propagating wave to have a plasmonic part. However, a compromise has to be found between the tight light confinement provided by the plasmonic effect, which we want to exploit to efficiently exalt the Kerr effect, and the propagation losses induced by the metal that can be too high and prevent the observation of the Kerr self-focusing. The chosen solution is to insert a thin silica buffer layer between the metal and the nonlinear dielectric layer. The designed waveguide including its plasmonic structure (PS) derives from our previously published theoretical studies [13,14] and from Finite Element Method simulations (Methods). To be more specific, the Kerr layer is constituted of a 3.6 μm thick Ge_{28.1} Sb_{6.3} Se_{65.6} amorphous chalcogenide thin film [23] (Fig. 1 a-b and Methods). This composition was chosen due to its large Kerr nonlinearity ($n_2 = 5.5 \cdot 10^{-18} \text{ m}^2/\text{W}$), moderate two-photon absorption coefficient ($\alpha_2 = 0.43 \text{ cm/GW}$) at the wavelength of interest of 1.55 μm , and a high damage threshold intensity evaluated to be at approximately 2.5 GW/cm^2 [22,24]. In addition, this film composition presents a reduced photo-sensitivity [24]. The silica buffer layer followed by a gold layer are then deposited on top. Finite Element Method (FEM) numerical simulations [25, 26] have been performed to compute the nonlinear

modes propagating in the structure in order to determine the optimum thicknesses for the top layers. These simulations showed that the silica buffer layer thickness d is the most critical parameter for the design, as expected from a previous study [27].

As shown in Fig. 2a for $d=30$ nm, the fundamental optical waves propagating in the structure are similar for TM and TE polarizations and resemble the modes present without metal. To the contrary, for $d=10$ nm, the TM mode clearly benefits from a strong localization due to the plasmonic effect while the TE mode is nearly unaffected (Fig. 2 and Methods). In addition, simulations show that a 10 nm buffer layer allows a decrease by a factor three of the propagation losses for the TM mode compared to a basic structure without silica buffer (see Supplementary information). Note that the deposition of a very thin SiO₂ layer of good quality is challenging with the operated sputtering deposition technique. To finalize the structure, a 32 nm thick gold layer was then sputtered on top, as illustrated in Fig. 1b. A cross section of the fabricated structure was analyzed by SEM (Fig. 1c), confirming that the targeted and fabricated nanolayer thicknesses are in accordance.

As depicted in Fig. 1d, the gold layer was patterned to obtain either rectangular or staircase (Fig. 1e) PS area. This arrangement provides the versatility to analyze several configurations by choosing the position of the launched beam along the Y-axis. For instance, propagation was tested with different PS lengths h and different PS locations. Specifically, three different PS locations were considered as described in Fig. 1d. The first one was a rectangular plasmonic pattern, $h = 660$ μm long, located at the exit face of the 5.1 mm long sample (configuration I). The two other configurations corresponded to a staircase PS with h varying from 100 μm to 500 μm , present either 1 mm before the exit face or 1mm after the entrance face to form configurations II and III, respectively from a 5.5 mm long sample. The input and output faces were formed by cleaving the processed wafer.

Optical characterizations

Optical characterizations were performed with a 1550 nm source emitting 200 fs pulses at a repetition rate of 80 MHz (Fig. 3a and Methods). The laser beam is elliptically shaped to form a 4 μm by 31 μm (Fig. 3a) beam waist (FWHM) along the X and Y-axes, respectively. It is end-fire coupled into the waveguide so that the 31 μm beam waist is located 2 mm inside the sample. Such an arrangement lowers the intensity at the entrance face compared to the intensity inside the waveguide. It thus helps to prevent input facet damage in the high intensity regime. In addition, it gives a weakly diffracting beam over the 5.1 mm long propagation distance. Careful beam alignment is also performed to maximize the beam overlap with the fundamental mode of the planar waveguide and thus avoid excitation of higher-order modes. Observation at the output face of the structure with a camera confirms that the presence of higher order modes is negligible. After the propagation inside the waveguide, the diffracted beam reaches a FWHM

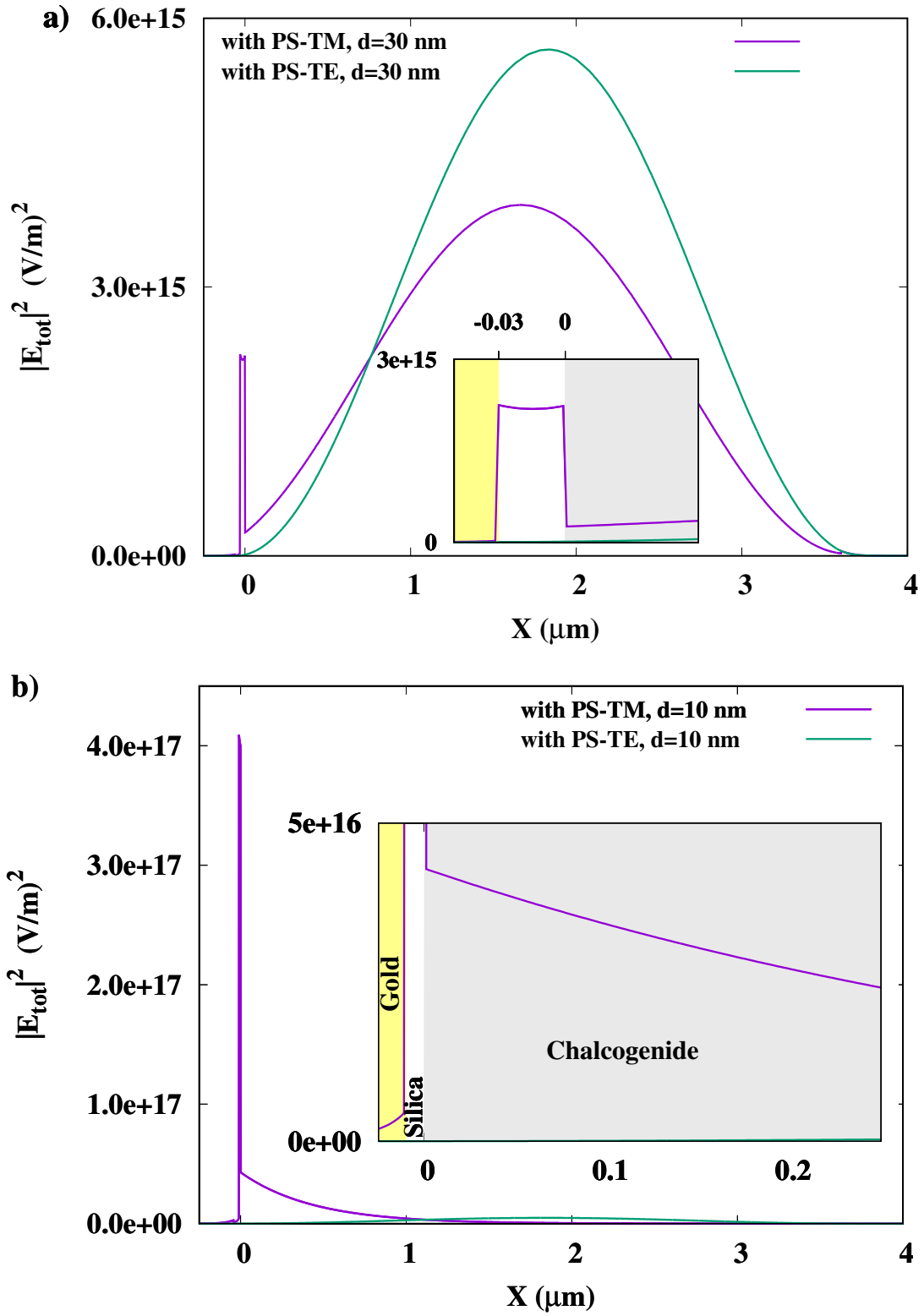


Figure 2: Calculated mode intensity profiles along the X-axis and zoom-in near the silica/gold interface(insets) of same power fundamental TM (green curves) and TE (magenta curves) for SiO_2 buffer thickness d equal to 30 nm (a) and 10 nm (b).

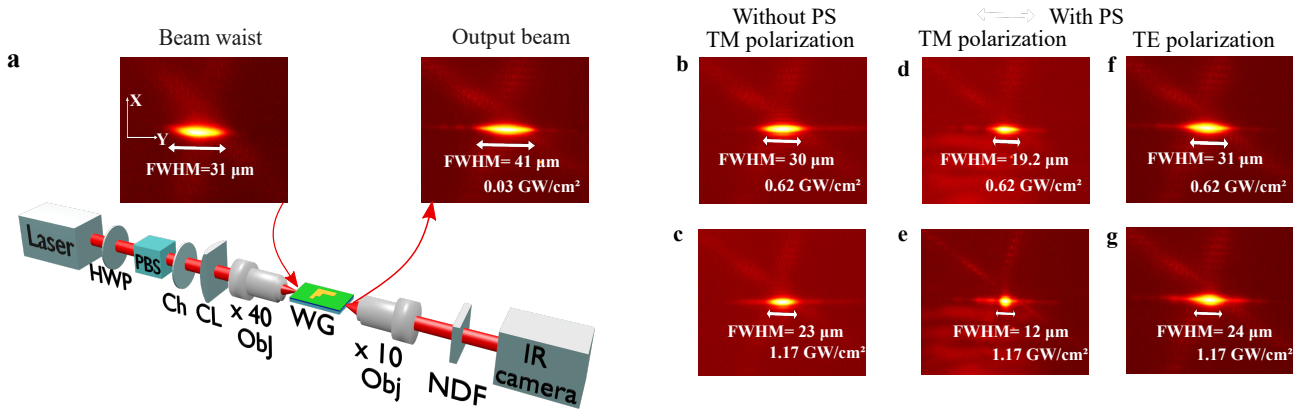


Figure 3: a, Experimental setup used for the observation of the plasmon-soliton wave and intensity distribution of the beam waist and output beam in linear regime. HWP; half wave plate, PBS; polarizing beam splitter, Ch; chopper, CL; cylindrical lens, Obj; microscope objective, NDF; neutral density filters. b–g, Intensity distribution of self-focused output beams for two input intensities without PS (b,c), with PS corresponding to configuration I for TM polarization (d,e) and for TE polarization (f,g).

of $41 \mu\text{m}$ along the Y-axis (Fig. 3a) in the linear regime (low intensity). In this regime a $\sim 21\%$ waveguide transmission is measured for both TM and TE polarizations when light propagates away from the metallized area. This transmitted power is consistent with a coupling efficiency of 28% and propagation losses of about 0.19 cm^{-1} .

To unambiguously reveal the influence of the plasmon-soliton wave on the beam self-focusing, we first characterize the self-trapping behaviour in the absence of metallic layer along the beam path. These preliminary experiments can thus be considered as a reference. As shown in references [21,22] the optical Kerr nonlinearity in similar chalcogenide slab waveguides can support spatial solitons at near-infrared wavelengths. In the tested sample we observe that, for an input intensity of 0.62 GW/cm^2 , a $30 \mu\text{m}$ FWHM beam is obtained at the output face (Fig. 3b). This size is close to the injected beam waist of $31 \mu\text{m}$ (Fig. 3a) which indicates that diffraction is compensated by the nonlinear Kerr self-focusing effect to form a spatial soliton [28].

A stronger focusing effect occurs if the input intensity is raised further. For an intensity of 1.17 GW/cm^2 a $23 \mu\text{m}$ FWHM is obtained at the output (Fig. 3c). Note that the very same behaviour is observed for both TM and TE polarizations for this configuration without PS. We then shift laterally the sample so that a PS is present on the trajectory of the launched beam. To be more specific, configuration I described in Fig. 1d is first considered with a PS length h of $660 \mu\text{m}$. In the linear regime the presence of this metallic structure located near the end of the waveguide does not modify the observed output beam distribution. The linear transmission is reduced however due to additional propagation losses compared to the situation

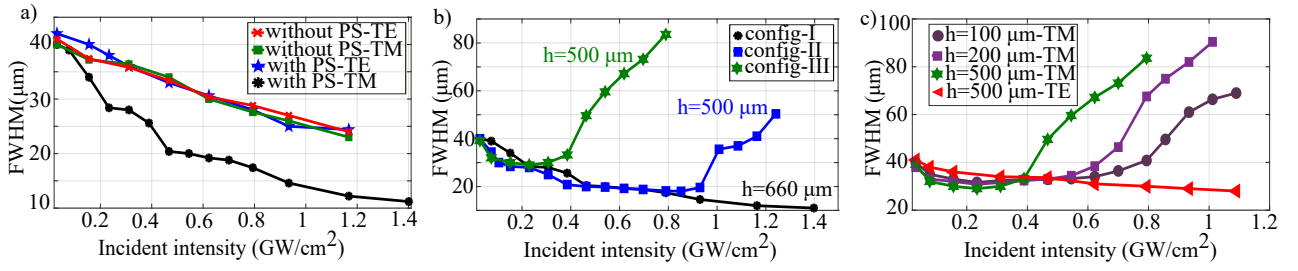


Figure 4: a, Measured output beam FWHM as a function of input intensity for both TM and TE polarizations without PS and with a PS corresponding to configuration I. b, Evolution of output beam FWHM as a function of input intensity for configurations I, II and III for TM polarization. c, Evolution of output beam FWHM for configuration III for PS lengths h of 500 μm , 200 μm and 100 μm for TM polarization and for h of 500 μm for TE polarization.

without the PS. We deduce that under the PS the attenuation is of 0.57 cm^{-1} and 28 cm^{-1} for TE and TM polarized light, respectively. The large attenuation for the TM case is a first indication of the plasmonic part of the plasmon-soliton predicted in Fig. 2b. Subsequently, as the intensity is raised, a strong enhancement of the self-focusing behaviour is observed at the output of the waveguide for TM waves. For instance, for an input intensity of 0.62 GW/cm^2 (Fig. 3d) the output beam is already narrower ($19\text{ }\mu\text{m}$ FWHM) than the injected one ($31\text{ }\mu\text{m}$ FWHM) while an even higher input intensity of 1.17 GW/cm^2 leads to a very efficient trapping of the beam, as witnessed by the output beam of $12\text{ }\mu\text{m}$ FWHM (Fig. 3e). By comparing this result with the one obtained at the same intensity without PS (Fig. 3c) we can deduce that the plasmonic enhanced nonlinear effect induced by the $660\text{ }\mu\text{m}$ long PS focuses the beam from about $23\text{ }\mu\text{m}$ to $12\text{ }\mu\text{m}$ FWHM. It is important to note that the exalted focusing is not observed for the TE polarization. Indeed, as shown in Fig. 3f-g, the TE wave shows no improved self-focusing compared to the configuration without the PS (Fig. 3 b-c). This polarization dependent behavior is a characteristic feature of the plasmonic effect on the field profile. To exclude the possible influence of thermally-induced self-focusing the experiment was repeated by inserting a mechanical chopper after the light source to diminish the average power to 40% while keeping the same peak power. We did not notice a measurable change compared to the behaviour described in Fig. 3 that excludes any significant role of the temperature (see Section 6 in Supplementary information).

The experimentally demonstrated striking self-focusing enhancement due to the plasmonic effect is also evident in the graph in Fig. 4a where the measured output FWHM beam is plotted as a function of the input beam intensity for TE and TM polarizations, both with and without the PS. For the three arrangements for which plasmon generation is not achievable, i.e. without or with PS for TE polarization, a similar behaviour is observed. This behaviour is characterized by a gradual focusing with a linear evolution of the beam width versus intensity. For a TM

polarized beam in presence of a PS, it differs significantly in this configuration I with $h=660 \mu\text{m}$. 1) We observe that this plasmon-enhanced configuration always gives rise to an output FWHM beam smaller than for the other three standard configurations. 2) The focusing effect takes place at a faster pace for low intensity. 3) Three times less intensity is required compared to the case without PS enhancement to obtain an output beam of similar size than the coupled beam waist of $31 \mu\text{m}$. 4) The FWHM evolves with a nonlinear trend and tends to saturate to a beam size approaching a narrow $11 \mu\text{m}$ FWHM value at high intensity ($1.4 \text{ GW}/\text{cm}^2$). Indeed, due to the linear and two photon absorptions, the intensity reaching the PS is not reduced as much as in configuration III where the PS is far from the input face.

To gain a better understanding of the disclosed plasmon-soliton wave that propagates within the PS and of the associated strongly enhanced focusing, additional configurations were tested. We first studied the influence of the position of the PS along propagation. Figure. 4b compares the observed FWHM as a function of intensity for a $500 \mu\text{m}$ long PS positioned either 1 mm before the exit face (Fig. 1d config. II) or 1 mm after the input face (Fig. 1d config. III) and the previously described case of the $660 \mu\text{m}$ long PS located at the exit face. At very low intensity the beam undergoes the same free diffraction in the 5.5 mm long sample regardless of the PS location, precluding any linear beam distortion from the PS. As soon as the intensity is raised the output beam focuses sharply in accordance with the Kerr-lens effect present in the PS. However, when the intensity is increased above an intensity threshold a spreading of the beam is observed for a PS located before the output face. The threshold is about $0.35 \text{ GW}/\text{cm}^2$ and $0.87 \text{ GW}/\text{cm}^2$ for a PS positioned 1 mm after the entrance face (config. III) or 1 mm before the exit face (config. II), respectively. This behaviour can once again be explained by the strong localized self-focusing induced by the PS. Indeed, when such a focusing leads to a narrow spot the beam diffraction cannot be compensated anymore by the weaker nonlinearity present after the PS and the beam diffraction is dominant. Consequently, beam spreading is observed at the output face. The diffraction is weaker in configuration II since the PS is only 1 mm from the output observation face. Note that, as observed experimentally, the input threshold intensity is expected to be weaker when the PS is close to the entrance face. Indeed, due to the linear and two photon absorptions, the intensity reaching the PS is not reduced as much as in configuration III where the PS is far from the input face.

To analyze the impact of the length h of the PS on the enhanced self-focusing observed for TM waves, experiments were conducted for PS lengths of $100 \mu\text{m}$ and $200 \mu\text{m}$ for configuration III (Fig. 1d-e). The results are presented in Fig. 4c along with measurements made for $h = 500 \mu\text{m}$ and for the enhancement free TE polarization. As the intensity increases, the PS self-focusing enhancement focuses the beam to a minimum value before a spreading of the FWHM occurs. The shorter the PS, the weaker the nonlinear focusing effect. The minimum beam size is reached at an intensity of about $0.24 \text{ GW}/\text{cm}^2$, giving an output FWHM of $31.6 \mu\text{m}$, $30.7 \mu\text{m}$ and $29 \mu\text{m}$ for $100 \mu\text{m}$, $200 \mu\text{m}$ and $500 \mu\text{m}$ PS length, respectively. As the intensity is

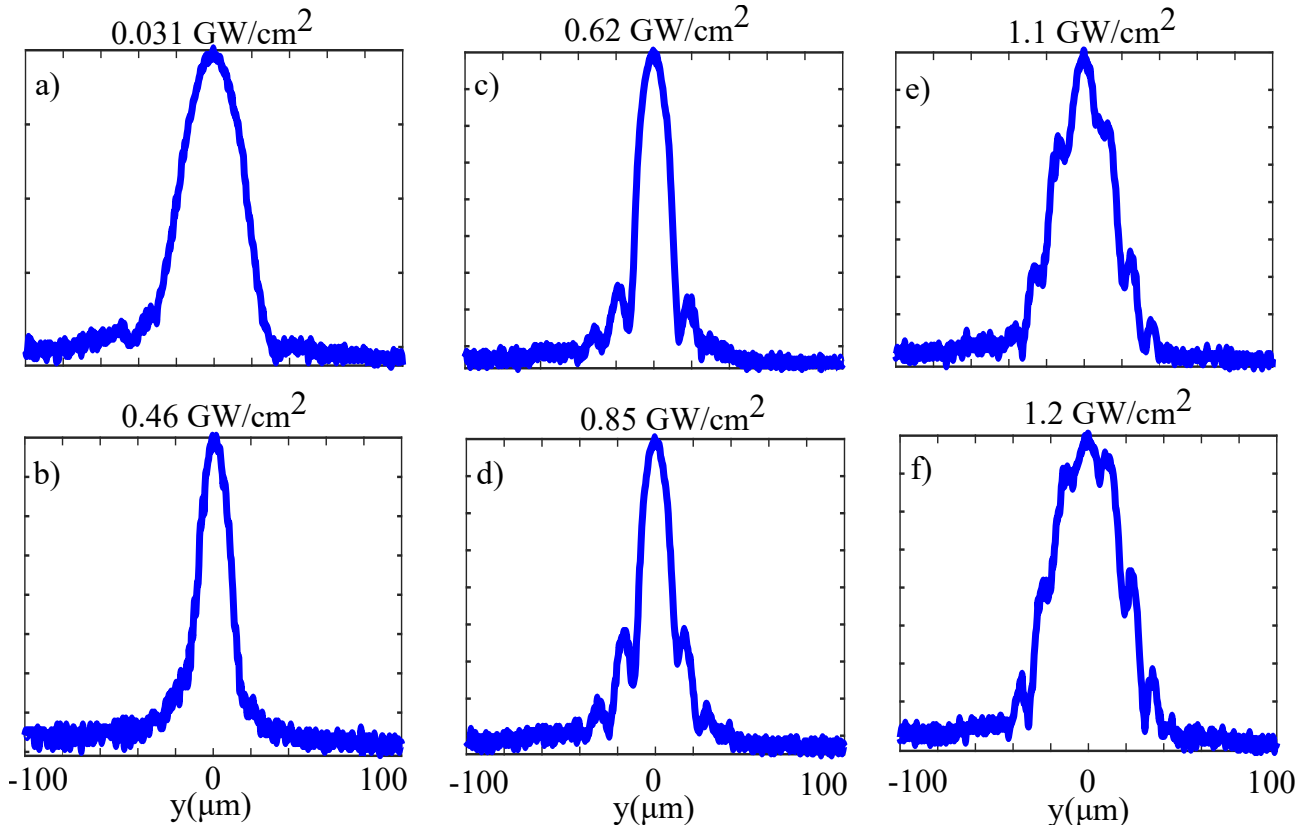


Figure 5: Output beam profile evolution as a function of incident intensity for configuration II, TM polarization, $h=500 \mu\text{m}$.

increased further, the defocusing occurs with a reverse dependency with the PS length: the shorter the PS length, the weaker the defocusing. This hints that even a PS as short as $100 \mu\text{m}$ can induce strong focusing.

An analysis of the output beam profile provides crucial additional information on the strong nonlinearity seen by the propagating beam that was not revealed by the FWHM measurements. In Fig. 5 the output beam profile is plotted for six intensity values for a $500 \mu\text{m}$ long PS positioned 1 mm from the output face (config. II). The efficient focusing effect described previously forms at first a smooth profile beam with a weak pedestal (Fig. 5b). This beam then enlarges and develops symmetric side lobes on both sides of the main peak as the intensity is raised (Fig. 5). This behaviour along with the plasmon enhanced self-focusing described above are corroborated by numerical calculations presented in the following section.

Simulations-Discussion

In order to confirm the plasmon-soliton propagation in the PS and to gain insight into the observed phenomena, we built a numerical scalar model based on a modified spatial nonlinear

Schrödinger equation (SNLSE). This model is adapted to take into account the mode field profile along the X-axis in the different sections of the full structure (Methods). Without PS, the field profiles of both TE and TM modes are nearly identical (Fig. 2a), and thus are the associated modal parameters. In contrast, in presence of a PS with a 10 nm thick SiO₂ layer, the propagation constants are slightly different (typically below 2% in the studied power range), but more importantly the field profiles are radically different. This dissimilarity gives at least a threefold enhancement of the effective nonlinearity parameter for the TM mode compared to the TE mode (See Supplementary information).

Fig. 6a presents the calculated profile evolution of the beam intensity from the SNLSE along the Y-axis versus propagation inside the full structure for the TM polarization for configuration II with $h = 500 \mu\text{m}$ at an input intensity (incident intensity $I=1.25 \text{ GW}/\text{cm}^2$) with the best numerically chosen enhancement factor for the effective nonlinearity (eight instead of three, see Supplementary information) that corresponds to the experiment depicted in Fig. 5f. This emblematic case reveals several remarkable characteristics that give more insight into the behaviour unveiled experimentally. First, we clearly see that the beam self-focuses along the first 2 mm in the structure and then it becomes nearly invariant before converging dramatically to a highly focused central peak as it travels in the 500 μm long PS region limited by the dashed lines. Finally, as the beam leaves this highly nonlinear PS region, diffraction supersedes the self-focusing effect. It is important to note that the numerical model also predicts the symmetric lateral peaks observed experimentally in Fig. 5. These peaks are generated in the last part of the PS for intensities above $0.6 \text{ GW}/\text{cm}^2$, in fair agreement with the experiments. Spatial modulation instability can be at the origin of the beam break-up of an initial noisy broad beam propagating in Kerr nonlinear media but it does not fit to the present phenomena. Indeed, the measured intensity dependence of the generated spatial frequency does not follow the scaling law of modulation instability [29,30]. Moreover, large amplitude spatial noise added in the present simulations does not give rise to the observed multi-peaks unless the plasmon-enhanced nonlinearity is present. We think the phenomenon described here is a combination of the beam break-up described in references [31,32] induced at the interface between a dielectric region with low Kerr-type nonlinearity and one with a high nonlinearity one and of the symmetric lateral peaks generated in overpowered spatial solitons in nonlinear full vector simulations (see Supplementary information).

The saturation of the self-focusing effect appearing at high power is also observed in the simulations. Discrepancies between theory and experiments remain. First, some limitations of the model can be invoked: it is based on a scalar SNLSE while the true problem is a vector one; paraxial approximations and calculation of the effective nonlinearity are not fully valid when the beam profile rapidly transforms in the PS; and the considered instantaneous response of the Kerr effect could be questioned in the femtosecond regime [33] (see Supplementary information). Second, there is some uncertainty on the values of the nonlinear coefficients n_2 and α_2 of this

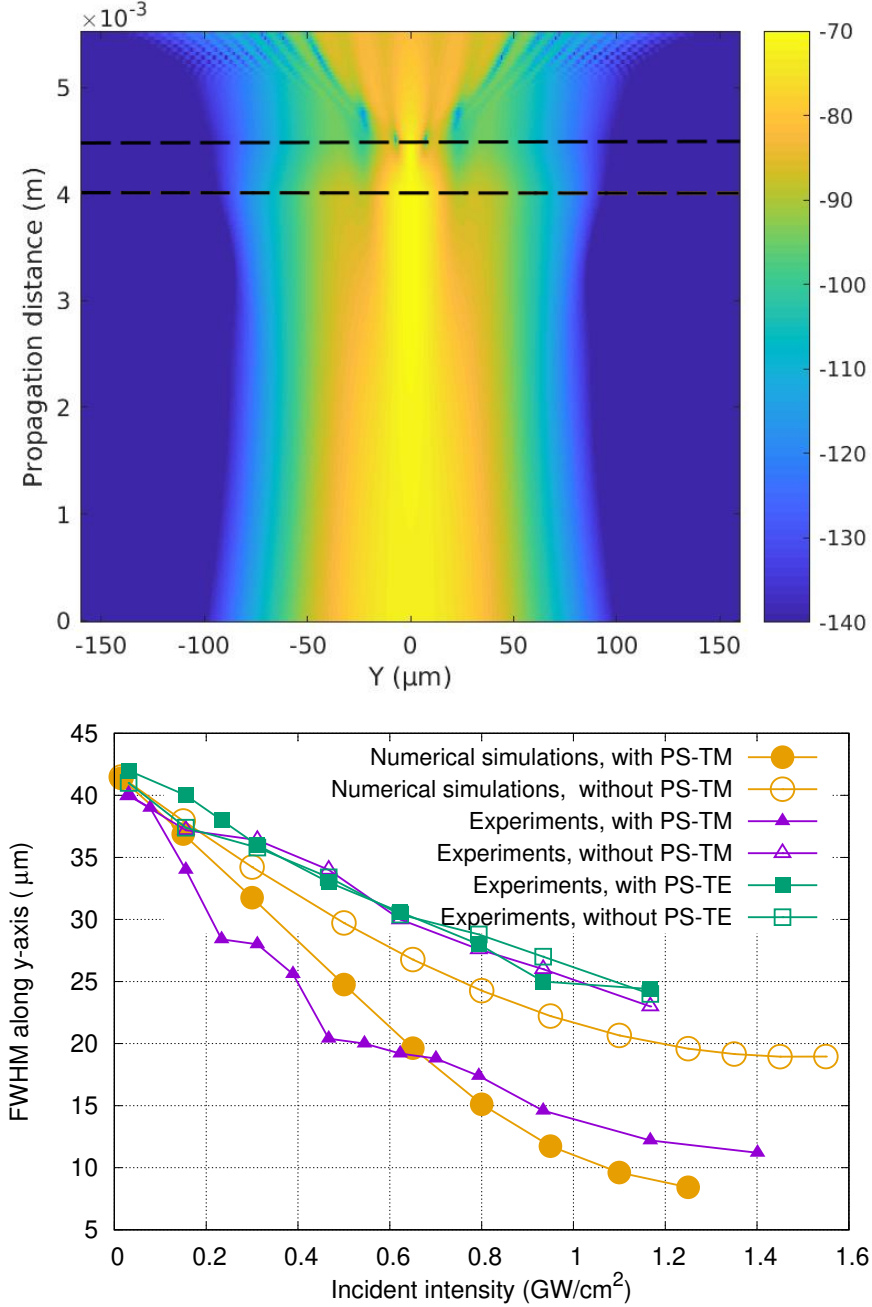


Figure 6: Numerical results. a, color map in log scale of the beam intensity evolution along the Y-axis versus propagation inside the full structure for the TM polarization for configuration II with $h = 500 \mu\text{m}$ in nonlinear regime (input incident intensity of $1.25 \text{ GW}/\text{cm}^2$). The dashed lines represent the limits of the PS. b, comparison of the computed and measured FWHM for configuration I as a function of the input beam intensity.

uncommon chalcogenide composition [34] (see also section B.1 in Supplementary information), and also on the exact values of the permittivity of the gold nanolayer and of its thickness along the plasmonic structure. Finally, potential nonlinear effects present in the gold layer [35-37]

can also be a reason of discrepancies between theory and measurements, especially in the high intensity regime.

Conclusion

In summary, a compelling spatial confinement of light observed only for TM polarization in a Kerr plasmonic structure arising from a plasmon-soliton wave has been demonstrated experimentally. The designed structure consists of a slab waveguide made of a highly nonlinear chalcogenide layer covered with nanolayers of silica and gold. The thickness of the silica layer has been tailored to benefit from the enhanced self-focusing due to the high-intensity plasmon while limiting the detrimental effect of propagation losses induced by the metal. Experimental observations are confirmed by numerical predictions obtained using an improved model of nonlinear propagation combining FEM modal results and spatial nonlinear Schrödinger equation. This first experimental proof validates the concept of the nonlinear spatial optical self-trapping enhanced by the assistance of a plasmon-soliton. It also allows envisioning the possibility of extending the demonstration to other nonlinear surface waves. In addition, the dramatic nonlinear beam reshaping induced over a distance of few hundreds microns at moderate light power also opens up new perspectives for nonlinear integrated plasmonic devices.

Acknowledgements

The authors would like to acknowledge the financial support of the Region Franche-Comté and of Aix-Marseille University, and of the Czech Science Foundation (project 16-17921S). This work was also partially supported by the FEMTO-ST MIMENTO technological facilities. We thank Tomáš Halenkovič for his contribution to the chalcogenide glass structure fabrication, Gwenn Ulliac for taking SEM image of the sample, and Xavier Romain for the graphics help.

Author contributions

G.R. proposed the experiment. G.R., M.C. and T.K. designed the PS structure. V.N., P. N. and N. C. fabricated the samples. T.K. performed the optical characterizations. G.R. and M.E. conducted the finite element method simulations, G.R. built the nonlinear propagation model and conducted the associated simulations. T.K. assisted with the results analysis. M.C. and G.R. provided in-depth discussion of the project and analyzed the results. M.C., G.R. and T.K. wrote the manuscript.

Methods

Structure fabrication

The heterostructure fabrication was realized in several steps. The chalcogenide glass target has been specially manufactured to accommodate RF sputtering magnetron deposition. First, a

3.6 μm thick $\text{Ge}_{28.1}\text{Sb}_{6.3}\text{Se}_{65.6}$ chalcogenide layer with a refractive index of 2.54 at 1.55 μm was deposited by RF magnetron sputtering method on an oxidized silicon wafer. The morphology and topography of the chalcogenide waveguides and heterostructure was characterized by SEM and AFM and showed no cracks with an RMS roughness of about 0.3 nm for chalcogenide films. The refractive index dispersion was determined by m-lines method and variable angle spectroscopic ellipsometry using Cody–Lorentz modelling. Then a 10 nm silica buffer layer is deposited by the sputtering technique followed by a 32 nm gold evaporated layer which is patterned by photolithography. The choice of a 32 nm thick gold nanolayer is a compromise between the need for a good quality layer with a constant thickness and the need to reduce the propagation losses generated by the metal knowing that the thinner the gold layer the smaller the losses.

Characterizations

Optical measurements were performed with an optical parametric oscillator emitting 200 fs pulses at a repetition rate of 80 MHz at 1550 nm (Chameleon OPO from Coherent). The power was varied by the combination of a half wave plate and a polarizer. The latter component is also used to adjust the polarization state of the injected beam to TM or TE polarization. An optical chopper can also be inserted to change the time average power. The laser beam is shaped into an elliptical spot using a cylindrical lens and a x40 microscope objective to form 4 μm and 31 μm beam waists (FWHM) along X-axis and Y- axis, respectively. The beam was end-fire coupled into the waveguide so that the 31 μm beam waist was located 2 mm inside the sample. The beam profile at the output of the sample was imaged on a Vidicon camera with a x10 microscope objective. Input and output powers were monitored by power meters to deduce the coupling efficiency, the peak power and the waveguide transmission. A coupling efficiency of 28% and propagation losses of about 0.19 cm^{-1} are measured away from PS structures. The input spatial averaged incident intensity was determined by dividing the coupled light peak power by the elliptical section of the guided mode at the entrance face corresponding to waists of 1.21 μm along the X-axis and 30 μm (35.5 μm FWHM) along the Y-axis.

Simulations

Modal analysis

Finite Element Method (FEM) numerical simulations [25,26] were performed to compute the nonlinear modes in the structures with PS in order determine the optimum thicknesses of the investigated layered structured. These simulations show that the silica buffer thickness d is the most critical parameter for the design as expected from previous studies [13,14,27]. As for all modal analysis, the investigated structure is assumed to be invariant along the propagation direction in the modeling.

As depicted in Fig. 2a, for a silica buffer layer thickness $d = 30$ nm, the TM and TE fundamental mode intensity profiles along the X-axis at a given power weakly differ. The presence of the metal marginally influences their distribution, as witnessed by the calculated

profiles which are very similar to the one of the fundamental guided modes of the silica (thick bottom layer)/chalcogenide slab waveguide. On the contrary, the TM mode profile is more and more affected by the metal as the silica buffer layer becomes thinner. For TM polarization, the studied metal/dielectric structure (Fig. 1 b) supports a plasmon-soliton wave that extends into the nonlinear dielectric layer. The propagation losses are weaker compared to the case of the extremely confined plasmonic waves present at a basic metal-dielectric interface. For our designed multilayer structure we expect plasmon propagation over a few hundreds micrometers. The plasmonic tail present in the nonlinear layer efficiently activates the Kerr effect. This configuration is thus favorable to reveal the formation of a self-focused beam that takes advantage of the plasmon-enhanced Kerr effect. Guided by our previously published theoretical studies [13,14,27], the FEM simulations provide an optimal value, in terms of nonlinearity enhancement and propagation losses, of 10 nm for the thickness of the silica buffer layer. It is worth mentioning that since the X and Y field profiles of the 2D plasmon-soliton nonlinear wave are coupled, the observed localization along the X axis (Fig. 2 b, TM polarization) is associated with an enhanced localization along the Y axis (See full profile view in Section 1 of the Supplementary information).

Propagation simulations

To study the propagation of the input beam along the full structure, as described in Fig. 1, which is no longer invariant along the Z direction we built a numerical model based on the spatial nonlinear Schrödinger equation (SNLSE) adapted to take into account the mode field profiles along X-axis in the full structure. This scalar model describes the transverse field profile along the Y-axis and its evolution versus propagation along the Z-axis [28]. The three different configurations (I, II, or III) including the different lengths h of the PS can be studied. The field dependency along the vertical X-axis does not explicitly appear in the model but is considered indirectly through the Z-dependent modal properties (effective nonlinearity and propagation constants) that appear in the SNLSE. These modal parameters are obtained from the FEM-based simulations of the main TE and TM modes associated with the different sections of the full structure [25,26]. Specifically, the effective nonlinearity is computed using several integrals of the computed modal field [26].

References

1. S. L. Cunningham, A. A. Maradudin, and R. F. Wallis, "Effect of a charge layer on the surface- plasmon-polariton dispersion curve," *Phys. Rev. B* 10, 3342 (1974).
2. S. A. Maier, *Plasmonics: Fundamentals and Applications* (Springer, 2007).
3. M. Kauranen and A. V. Zayats, "Nonlinear plasmonics," *Nat. Photonics* 6, 737 (2012).

4. H. J. Simon, D. E. Mitchell, and J. G. Watson, "Optical Second-Harmonic Generation with Surface Plasmons in Silver Films," *Phys. Rev. Lett.* 33, 1531–1534 (1974).
5. M. Z. Alam, J. S. Aitchison, and M. Mojahedi, "A marriage of convenience: Hybridization of surface plasmon and dielectric waveguide modes," *Laser Photonics Rev.* 8, 394–408 (2014).
6. V. M. Agranovich, V. Babichenko, and V. Y. Chernyak, "Nonlinear surface polaritons," *JETP Lett* 32, 512–515 (1980).
7. W. J. Tomlinson, "Surface wave at a nonlinear interface," *Opt. Lett.* 5, 323–325 (1980).
8. J. Ariyasu, C. T. Seaton, G. I. Stegeman, A. A. Maradudin, and R. F. Wallis, "Nonlinear surface polaritons guided by metal films," *J. Appl. Phys.* 58, 2460–2466 (1985).
9. N. N. Akhmediev, "Novel class of nonlinear surface waves: asymmetric modes in a symmetric layered structure," *Sov Phys JETP* 56, 299–303 (1982).
10. E. Feigenbaum and M. Orenstein, "Plasmon- soliton," *Opt. Lett.* 32, 674–676 (2007).
11. A. R. Davoyan, I. V. Shadrivov, and Y. S. Kivshar, "Self-focusing and spatial plasmon-polariton solitons," *Opt. Express* 17, 21732–21737 (2009).
12. K. Y. Bliokh, Y. P. Bliokh, and A. Ferrando, "Resonant plasmon-soliton interaction," *Phys. Rev. A* 79, 041803 (2009).
13. W. Walasik, V. Nazabal, M. Chauvet, Y. Kartashov, and G. Renversez, "Low-power plasmon-soliton in realistic nonlinear planar structures," *Opt. Lett.* 37, 4579–4581 (2012).
14. W. Walasik, G. Renversez, and Y. V. Kartashov, "Stationary plasmon-soliton waves in metal-dielectric nonlinear planar structures: Modeling and properties," *Phys. Rev. A* 89, 023816 (2014).
15. W. Walasik and G. Renversez, "Plasmon-soliton waves in planar slot waveguides. I. Modeling," *Phys. Rev. A* 93, 013825 (2016).
16. W. Walasik, G. Renversez, and F. Ye, "Plasmon- soliton waves in planar slot waveguides. II. Results for stationary waves and stability analysis," *Phys. Rev. A* 93, 013826 (2016).
17. A. Marini and F. Biancalana, "Ultrashort Self- Induced Transparency Plasmon Solitons," *Phys. Rev. Lett.* 110, 243901 (2013).
18. D. A. Smirnova, I. V. Shadrivov, A. I. Smirnov, and Y. S. Kivshar, "Dissipative plasmon-solitons in multilayer graphene", *Laser Photonics Rev.* 8, No. 2, 291–296 (2014)

19. M. L. Nesterov, J. Bravo-Abad, A. Nikitin, F. J. Garcia-Vidal, and L. Martin-Moreno, "Graphene supports the propagation of subwavelength optical solitons", *Laser Photonics Rev.* 7, No. 2, L7–L11 (2013)
20. A. Pusch, I. V. Shadrivov, O. Hess, and Y. S. Kivshar, "Self-focusing of femtosecond surface plasmon polaritons," *Opt. Express* 21, 1121–1127 (2013).
21. M. Chauvet, G. Fanjoux, K. P. Huy, V. Nazabal, F. Charpentier, T. Billeton, G. Boudebs, M. Cathelinaud, and S.-P. Gorza, "Kerr spatial solitons in chalcogenide waveguides," *Opt. Lett.* 34, 1804–1806 (2009).
22. T. Kuriakose, E. Baudet, T. Halenkovic, M. M. R. Elsayy, P. Nemeč, V. Nazabal, G. Renversez, and M. Chauvet, "Measurement of ultrafast optical Kerr effect of Ge–Sb–Se chalcogenide slab waveguides by the beam self-trapping technique," *Opt. Commun.* 403, 352–357 (2017).
23. V. Nazabal, F. Charpentier, J.-L. Adam, P. Nemeč, H. Lhermite, M.-L. Brandily-Anne, J. Charrier, J.-P. Guin, and A. Moréac, "Sputtering and Pulsed Laser Deposition for Near- and Mid-Infrared Applications: A Comparative Study of Ge₂₅Sb₁₀S₆₅ and Ge₂₅Sb₁₀Se₆₅ Amorphous Thin Films: Sputtering and Pulsed Laser Deposition for Near- and Mid-IR Applications," *Int. J. Appl. Ceram. Technol.* 8, 990–1000 (2011).
24. M. Olivier, J.C. Tchahame, P. Nemeč, M. Chauvet, V. Besse, C. Cassagne, G. Boudebs, G. Renversez, R. Boidin, E. Baudet, and V. Nazabal, "Structure, nonlinear, properties, and photosensitivity of (GeSe₂)_{100-x}(Sb₂Se₃)_x glasses", *Opt. Mat. Expr.*, 4, 525-540 (2014).
25. M. M. R. Elsayy and G. Renversez, "Study of plasmonic slot waveguides with a nonlinear metamaterial core: semi-analytical and numerical methods", *Journal of Optics*, 19, 075001 (2017).
26. M. M. R. Elsayy and G. Renversez, "Exact calculation of the nonlinear characteristics of 2D isotropic and anisotropic waveguides," *Opt. Lett.* 43, 2446-2449 (2018).
27. M. M. R. Elsayy and G. Renversez, "Improved nonlinear slot waveguides using dielectric buffer layers: properties of TM waves", *Opt. Lett.*, 41, pp. 1542-1545 (2016).
28. S. Trillo and W. Torruellas (eds), *Spatial Solitons, SSOS*, volume 82, Springer 2001.
29. R. Malendevich, L. Jankovic, G. Stegeman, and J. S. Aitchison, "Spatial modulation instability in a Kerr slab waveguide," *Opt. Lett.* 26, 1879–1881 (2001).
30. Y. Y. Lin, R. K. Lee, and Y. S. Kivshar, "Transverse instability of transverse-magnetic solitons and nonlinear surface plasmons," *Opt. Lett.* 34, 2982–2984 (2009).

31. A. B. Aceves, J. V. Moloney, and A. C. Newell. “Theory of light-beam propagation at nonlinear interfaces. II. Multiple-particle and multiple- interface extensions”, *Phys. Rev. A* 39, 1828 (1989).
32. J. Sánchez-Curto, P. Chamorro-Posada, and G. S. McDonald, “Bright and black soliton splitting at nonlinear interfaces”, *Phys. Rev. A* 85, 013836 (2012).
33. C. Cambournac, H. Maillotte, E. Lantz, J. M. Dudley, M. Chauvet, “Spatiotemporal behavior of periodic arrays of spatial solitons in a planar waveguide with relaxing Kerr nonlinearity”, *J. Opt. Soc. Am. B*, 19, 574-585 (2002).
34. G. Boudebs, S. Cherukulappurath, H. Leblond, J. Troles, F. Smektala, F. Sanchez, “Experimental and theoretical study of higher-order nonlinearities in chalcogenide glasses”. *Opt. Comm.*, 219, 427-433 (2003).
35. R. W. Boyd, Z. Shi, I. De Leon, “The third-order nonlinear optical susceptibility of gold”, *Opt. Comm.*, 326, 74-79 (2014).
36. H. Qian, Y. Xiao, Z. Liu, “Giant Kerr response of ultrathin gold films from quantum size effect”, *Nat. Commun.* 7, 13153 (2016).
37. A. Tuniz, S. Weidlich, M. A. Schmidt, “Effectively Single-Mode Self-Recovering Ultrafast Nonlinear Nanowire Surface Plasmons”, *Phys. Rev. Appl.* 9, 044012 (2018).

Supplementary information of the article "Experimental demonstration of plasmon-soliton waves"

Contents

A	Details of the nonlinear mode profiles	19
A.1	Impact of the thickness d of the silica buffer on the nonlinear mode type	19
A.2	Impact of the total power on the nonlinear modes	19
B	Details of the solved nonlinear propagation equation	20
B.1	Model and equations	20
B.2	Numerical implementation	24
C	Impact of parameter variability for the simulations of configuration I	25
C.1	Influence of silica buffer layer thickness d	25
C.2	Influence of n_2 and of the ratio $\eta_x^{1D}(\text{TM with PS})/\eta_x^{1D}(\text{TM without PS})$	25
D	Complementary results for configuration II	26
D.1	Propagation simulations for configuration II at low power	26
D.2	Comparisons between experimental results and numerical simulations for configuration II as a function of the PS length	27
E	Complementary results for configurations I, II, and III	29
F	Discussion on the limitations of the SNLSE	30
G	Test of thermal effects	31
	References	32

A Details of the nonlinear mode profiles

We can compute the nonlinear vector modes that propagate in a waveguide or photonic structure with a Kerr nonlinearity region as a function of the mode power using the model we have already developed using the finite element method (FEM) and the fixed power algorithm [1] (see the Methods section in the main article) based on Maxwell's equations. In this section we focus on two issues: the impact of the thickness d of the silica buffer layer between the gold layer and the chalcogenide nonlinear layer on the type of modes, and the impact of the power carried by the nonlinear solution on the modes distribution.

A.1 Impact of the thickness d of the silica buffer on the nonlinear mode type

As already stated (see main article and quoted references), the thickness d of the silica buffer plays a key role in the mode type independently of the considered linear or nonlinear regimes. In Fig. 2 of the main article, only profiles of the modulus squared of the electric field (intensity) along the X-axis for $y = 0$ are provided for the main TE and TM modes for two silica buffer thicknesses d . In Fig. 7, a 3D view of the intensity profiles of the nonlinear modes with the same carried total power for $d = 10$ nm and $d = 30$ nm is given.

First, Figure 7 shows the 2D localization of the investigated modes induced by the nonlinearity especially along the Y axis despite the absence of any permittivity contrast in this direction in the initial structure. Second, this figure also clearly illustrates the stronger localization of the electric field of the TM mode for a PS with a silica buffer layer of $d = 10$ nm thickness (see Fig. 8 for a full view of this TM mode) compare to a PS with $d = 30$ nm. It is this stronger spatial localization for both along the X-axis and the Y-axis that makes the improvement of the effective nonlinearity for the TM mode in presence of the PS compare to the ones of the three other cases studied experimentally in the main article: TM mode without PS, TE mode with and without PS.

For completeness, in Fig. 9, we provide a full 3D view of the intensity profiles of the TM and TE nonlinear modes for the same total power of $P_{tot} = 513$ W for $d = 30$ nm. One can see that both polarizations have similar features in term of localization as stated in the main article.

A.2 Impact of the total power on the nonlinear modes

In nonlinear regime (at high intensity), the shape of the mode field profiles depends on the carried power. Two normalized intensity profiles of the nonlinear TM modes computed for $P_{tot} = 513$ W and $P_{tot} = 1108$ W are shown in Fig. 10.

Along the X-axis, the mode width dependence on power is weak since it is mainly dictated

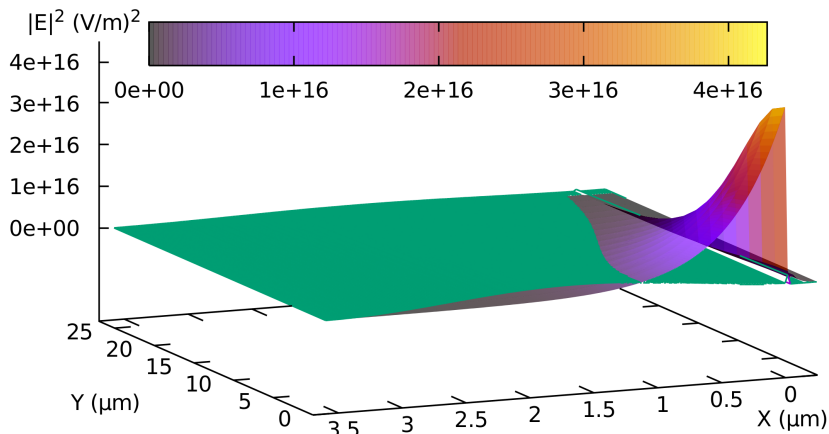


Figure 7: Intensity distribution of the nonlinear TM modes (only one half shown thanks to the symmetry axis along $y = 0$) for $d = 10$ nm (with color scale) and for $d = 30$ nm (green) with the same total power $P_{tot} = 513$ W. The vertical scale is identical for the two modes. Note that for $d=10$ nm, the distribution in the silica buffer layer is not shown due to its large value as shown in the profile provided in Fig. 2 of the main article. See Fig. 8 for the view of the distribution in the full structure.

by the layers layout (see Table 1 in the next section for a quantitative impact of this power dependence). The impact of power on the Y-axis FWHM is stronger but there is no need to insert this width in the propagation equation (3) since this equation describes by itself the focusing effect along the Y-axis due to the nonlinearity. Note that these FEM results cannot be compared directly with the experimental ones. Indeed, experimentally the propagation also includes the progressive beam reshaping toward a soliton profile since the input beam is fairly focused on the input facet of the structure and does not correspond to the self-coherent solution corresponding to the computed nonlinear modes.

B Details of the solved nonlinear propagation equation

B.1 Model and equations

With our propagation simulations using a SNLSE (spatial nonlinear Schrödinger equation), we want to predict the spatial profile along Y-axis versus propagation along the Z-axis taking into account the spatial profile along the X-axis of the nonlinear mode in the studied region of the structure. To realize this task, we consider that the structure is step-wise constant along the Z-axis. In each discretized segment of the propagation, we determine the main mode using our

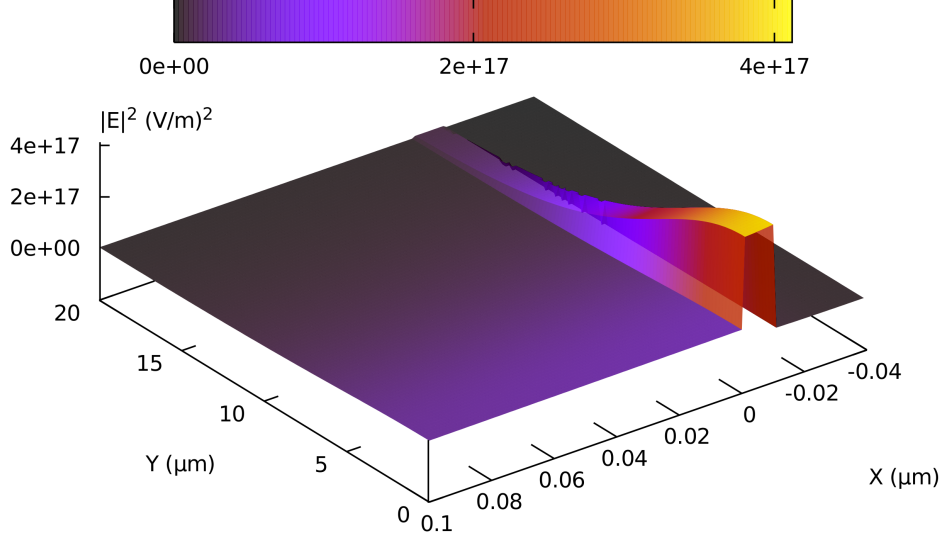


Figure 8: Intensity distribution of the nonlinear TM modes propagating inside the full PS for $d=10$ nm with a total power $P_{tot} = 513$ W (only one half shown thanks to the symmetry axis along $y = 0$). Note that due to the large values of the intensity in the silica buffer layer, the intensity in the other regions are not well resolved (see Fig. 7 for details of these regions.)

FEM mode solver (see Methods. Simulations. Modal Analysis). The mode XY-distribution is determined together with its propagation constant in each segment.

It is worth to remind that usually in basic spatial solitons studies [2, 3] only one transverse dimension is considered. In the present study since we need to take into account the spatial field profile along the X-axis that differs for the dielectric type mode profiles and for the plasmonic type mode profile obtained only for the TM polarization with PS, we start from the nonlinear evolution equation where both x and y variables are considered. To get the final SNLSE involving only the transverse coordinate y and the propagation direction coordinate z , we proceed in a similar way as it is done when the NLSE is derived in the temporal domain using a spatial integration in the cross section of the waveguide [4]. This study differs since we limit the spatial integration to the nonlinear region of the X-axis to keep the dependency along the Y-axis. We also renormalize the investigated amplitude denoted by $\tilde{A}(y, z)$ in order to get directly the optical intensity I when one takes its modulus squared.

$$\mathbf{E}(\mathbf{r}, t) = \frac{1}{2} \hat{\mathbf{u}} (F(x)A(y, z) \exp(-i(\omega_0 t - \beta_0 z)) + cc) \quad (1)$$

$$|\tilde{A}(y, z)|^2 = |A(y, z)|^2 \frac{2}{\varepsilon_0 n c} \quad (2)$$

where cc means the complex conjugate and $\hat{\mathbf{u}}$ is a fixed unitary vector in the waveguide cross-

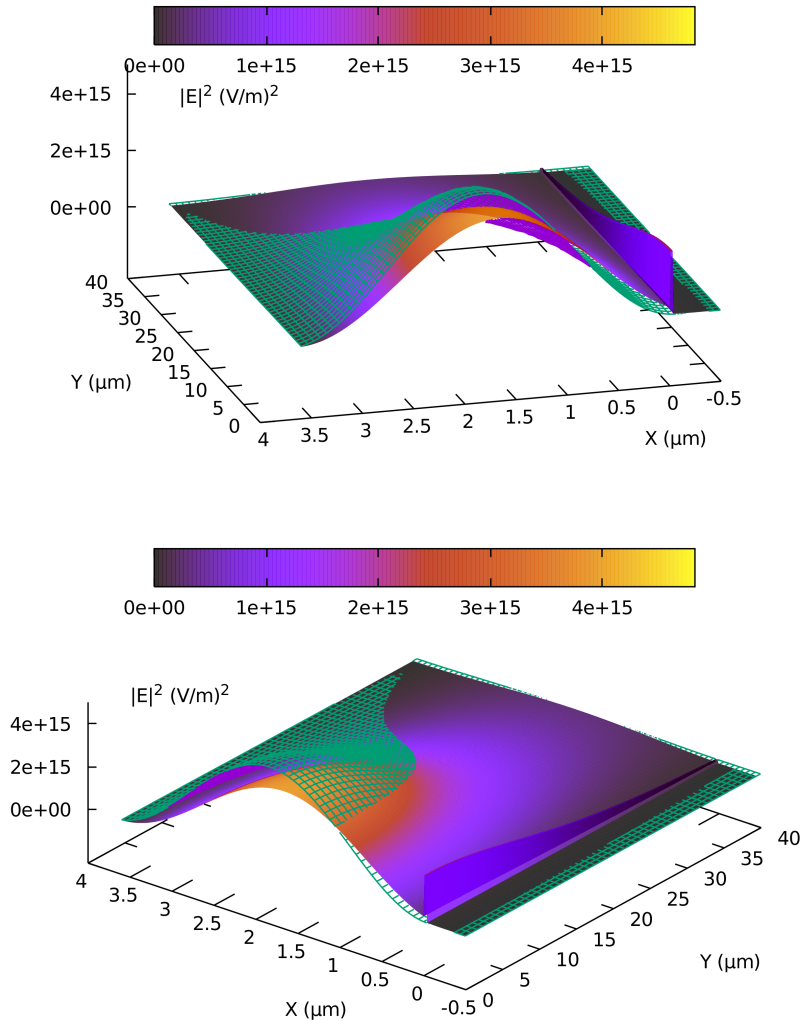


Figure 9: Intensity profiles of the nonlinear TM and TE modes for $d = 30$ nm and a power $P_{tot} = 513$ W seen from two view-points. The TM mode is shown with the color scale while the TE mode is shown using the green mesh. The vertical scale is the same for the two modes.(only one half shown thanks to the symmetry axis along $y = 0$)

section depending on the studied polarization. $\tilde{A}(y, z)$ obeys the following SNLSE:

$$\frac{\partial \tilde{A}(y, z)}{\partial z} = \frac{i}{2\beta_0} \frac{\partial^2 \tilde{A}(y, z)}{\partial y^2} - \frac{\alpha}{2} \tilde{A}(y, z) - \frac{\alpha_2}{2} |\tilde{A}(y, z)|^2 \tilde{A}(y, z) + \frac{i\omega_0 n_2}{c} \eta_x^{1D} |\tilde{A}(y, z)|^2 \tilde{A}(y, z) \quad (3)$$

with

$$\eta_x^{1D} \equiv \int_{\text{NL layer}} F(x)^4 dx / \int_{\text{NL layer}} F(x)^2 dx \quad (4)$$

where $F(x)$ is the normalized spatial profile along x of the mode of interest in the considered segment of the structure, α is the linear loss coefficient, α_2 the two-photon absorption nonlinear coefficient, and n_2 the Kerr nonlinear coefficient of the chalcogenide layer. The one-dimensional integrals defining η_x^{1D} are computed only in the nonlinear region. These integrals are computed using our FEM mode solver as the propagation constant β_0 and the full field profiles.

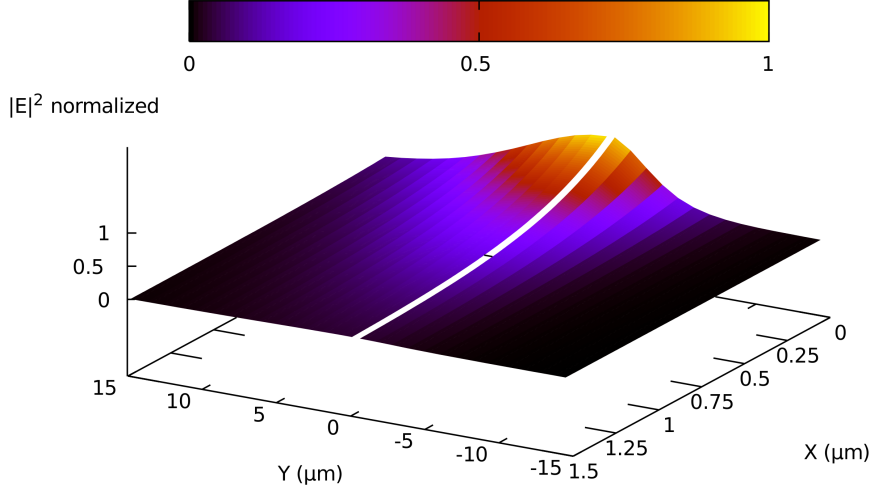


Figure 10: Normalized intensity distribution of the nonlinear TM modes for two different powers P_{tot} for $d = 10$ nm: $P = 513$ W on the left part (positive Y), $P = 1026$ W on the right (negative Y). (only one half shown thanks to the symmetry axis along $y = 0$)

We call this η_x^{1D} parameter the opto-geometrical nonlinear factor. Before pursuing the description of the η_x^{1D} quantity, it is needed to explain how the experimental value of the material nonlinear coefficient n_2 has been obtained. In several cases, its value is derived from nonlinear propagation simulations using the two-dimensional spatial nonlinear Schrödinger equation where the transverse FWHM is computed and then compared to the measured ones as we have already done in reference [5] but the used equation did not take into account the field profile along the X-axis (axis perpendicular to the layer) and consequently the factor η_x^{1D} was missing. The used equation was actually the equation describing the spatial variation of an optical beam during the nonlinear propagation only in one transverse direction but not within a 2D cross section structure. If we compare these two equations (Eq. (1) in reference [5], or equivalent equation given in [3] with Eq. (3) given in this Section B), one can see that the η_x^{1D} factor describing the field profile in the direction perpendicular to the propagation axis (Z) and to the axis associated with the second spatial coordinate of the SNLE (Y) appears only in the last term of Eq. (3). This factor η_x^{1D} is similar to the η one described in the derivation of the nonlinear Schrödinger equation in the temporal domain for optical fibers by formula (5.26) in Okamoto's book [6]. But in this later case, the spatial integration is realized on the full 2D cross section (not only on the nonlinear fiber core) in order to approximate its value by a factor 1/2 for the HE_{11} mode of a circular step-index fiber under the normal operating condition of such fiber. This is not the case in our study where we integrate only along the dimension (X-axis) corresponding to the thickness of the nonlinear layer. The values of η_x^{1D} for the studied structures, for the main TE and TM modes with and without the PS are given in Table 1. These values are computed

P_{tot} (W)	513	1108	2216
TM with PS	1.23	1.26	1.37
TE with PS	0.40	0.40	
TM without PS	0.39	0.39	0.39
TE without PS	0.40	0.40	
ratio: TM with PS/ TM without PS	3.15	3.23	3.51

Table 1: Opto-geometrical nonlinear factor η_x^{1D} , for the main TE and TM modes with and without the PS for several values of the mode total power and a silica buffer layer thickness $h = 10$ nm.

using the nonlinear fixed power algorithm described in reference [1], see also Section A of this Supplementary information and the Methods Section (Simulations. Modal Analysis) of the main article.

The TE mode without PS and TM mode without PS correspond to the cases used to evaluate the nonlinear coefficient n_2 in reference [5]. As a result, the previously provided n_2 takes into account the mode related quantity η_x^{1D} for the TE and TM cases without PS, its value is numerically evaluated to approximately 0.4. For the TM mode with PS, η_x^{1D} is between 3 and 3.4 times higher than for the other cases. It slightly increases with the mode power as shown in Table 1. Consequently, the effective nonlinearity improvement for the TM mode with PS is at least three fold the ones without plasmonic enhancement. We found that in order to quantitatively reproduce the different experimental results for the three experimentally tested configurations (I, II, and III) we have to use an opto-geometrical nonlinear factor not three times higher, as evaluated by the FEM simulations, but eight times higher. We mainly attribute this discrepancy to our modelling approach (see Section F in this document and the last paragraph of the section Simulation-Discussion of the main article). In other words, our modelling approach underestimates the observed nonlinearity in the TM case with PS. Among possible explanations, we didn't take into account the gold nonlinearity. It is worth pointing out that in the linear regime our simulations recover the expected results from linear Gaussian beam propagation.

B.2 Numerical implementation

We solve Eq. (3) using the Runge Kutta method of order 4 with the Interaction Picture (RK4IP) method, initially designed to solve the NLSE in the temporal domain, but adapted in the present case to the spatial domain since the RK4IP method has been proven to be more accurate and more efficient than the split-step Fourier method [7]. This task is relatively straightforward since there is no spatial dispersion to take into account due to the fact that we

investigate only the beam propagation at a single wavelength ($1.55 \mu\text{m}$) while to solve the time equation one must take into account the frequency dependency of material properties to get accurate results. In addition to improve the efficiency of our numerical implementation, we have used the local error adaptative step size method that allows to adapt continuously the spatial step size in the propagation direction but keeping the local error below a fixed threshold [8]. We have already used it successfully to study supercontinuum generation in highly nonlinear chalcogenide microstructured optical fibers [9].

C Impact of parameter variability for the simulations of configuration I

In this section, we describe the impact of parameters values on the simulations results describing configuration I.

C.1 Influence of silica buffer layer thickness d

We describe the influence of the silica buffer thickness when it is below the critical size ensuring a plasmonic behaviour for the TM mode with the PS. The targeted thickness d of 10 nm was obtained in the fabricated sample (see Fig. 1c in the main article). Nevertheless, it is possible that this thickness d is not constant along the fabricated PS. For instance, if $d = 8$ nm instead of 10 nm, the corresponding mode for $P=513$ W changes compared to the one computed for $d = 10$ nm: the η_x^{1D} is now equal to 1.56 instead of 1.23. This implies that the ratio $\eta_x^{1D}(\text{TM with PS})/\eta_x^{1D}(\text{TM without PS})$ increases from 3.2 to 4. Consequently, the effective nonlinearity is increased when d decreases from 10 nm to 8 nm.

C.2 Influence of n_2 and of the ratio $\eta_x^{1D}(\text{TM with PS})/\eta_x^{1D}(\text{TM without PS})$

In Fig. 11, the FWHM is computed from nonlinear propagation simulations for configuration I as a function of the input beam intensity for several sets of n_2 and ratio $\eta_x^{1D}(\text{TM with PS})/\eta_x^{1D}(\text{TM without PS})$ values including the one given in Fig. 6b of the article (purple curves shown in Fig. 11). As stated in ref. [22], for a GeSbSe chalcogenide glass of similar composition and for an identical laser source as in the present study, the estimated uncertainty on n_2 is 28.5%. This statement induces that the n_2 value is typically in the interval $[4 - 7] 10^{-18} \text{ m}^2/\text{W}$. One can see that the simulation results differ only quantitatively and that the FWHM variations stay in the correct range. To simplify the discussion in the article, we use the n_2 value provided by the corrected results from reference [22] *i.e.* $5.5 10^{-18} \text{ m}^2/\text{W}$ but one can see that if we choose $4.5 10^{-18} \text{ m}^2/\text{W}$, we obtain simulation results (green curves in Fig. 11) nearest to the

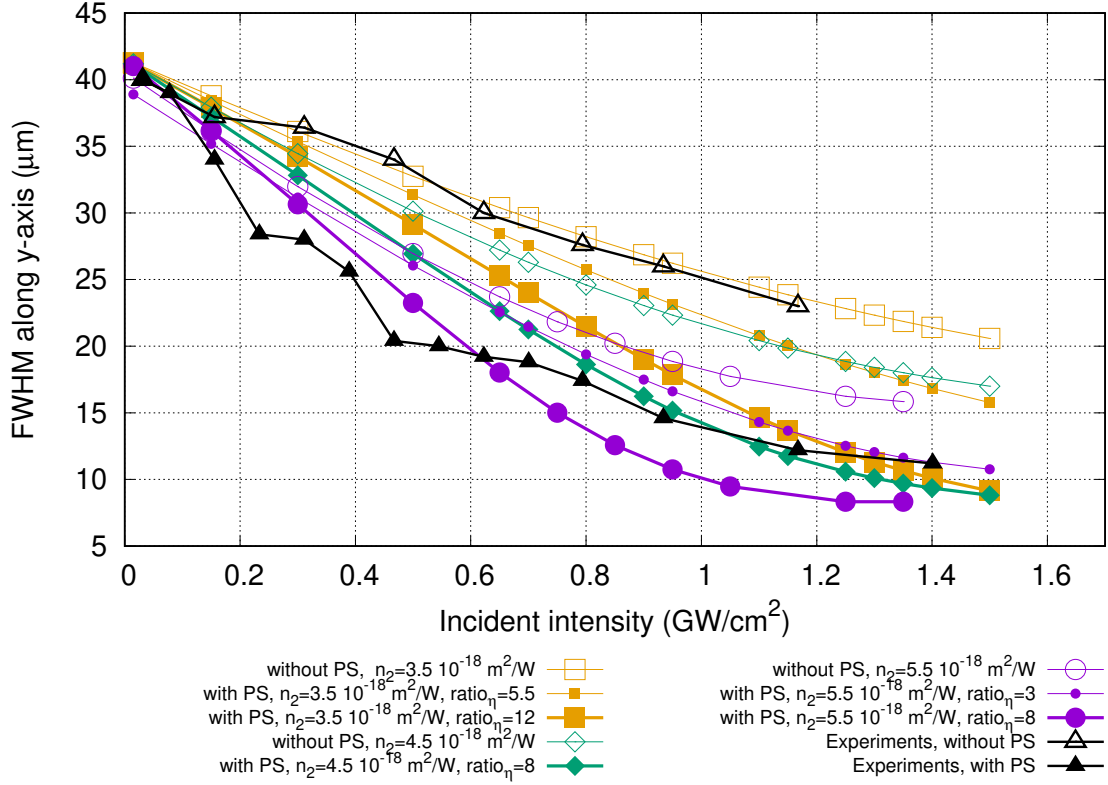


Figure 11: Comparison of the computed FWHM for configuration I as a function of the input beam intensity for several sets of n_2 and $\eta_x^{1D}(\text{TM with PS})/\eta_x^{1D}(\text{TM without PS})$ ratio values, the experimental results are also shown in black for the TM case with (filled triangles) and without PS (empty triangles).

experimental results (black curves in Fig. 11).

D Complementary results for configuration II

D.1 Propagation simulations for configuration II at low power

In Fig. 5, we provide a color map of the beam intensity evolution along the Y-axis versus propagation distance inside the full structure for the TM polarization for configuration II with $h=500 \mu\text{m}$ for an input average intensity of $1.25 \text{ GW}/\text{cm}^2$.

In order to complete these results and to validate the effect of the input intensity an additional color map is given in Fig. 12 for same parameters except an input incident average intensity of $15 \text{ MW}/\text{cm}^2$.

In this figure, one can first see the focusing of the input beam on the initial section of the full structure (before the PS). This weak focusing is mainly due to the phase profile of the input beam [3] since we must impose a spatial chirp to take into account the beam focusing induced by the microscope objective used to couple light in the structure.

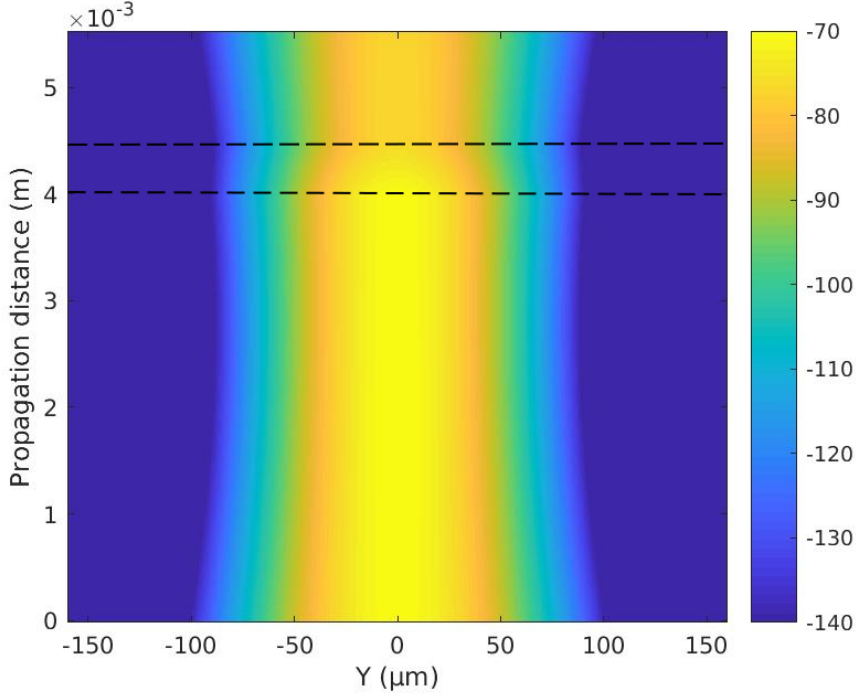


Figure 12: Color map in log scale of the beam intensity profile along the Y-axis versus propagation coordinate inside the full structure for a TM polarization for configuration II with $h=500 \mu\text{m}$. Input intensity of $15 \text{ MW}/\text{cm}^2$. The dotted line represents the limits of the PS.

Second, a focusing effect is visible under the PS structure region attributed to the enhanced nonlinearity. Note that such a self-focusing takes place even for such a low intensity. Third, as the beam exits from the PS, a defocusing occurs due to the combination of the power loss induced by the higher propagation losses in the PS region and of the enhancement-free nonlinearity present away from the PS.

D.2 Comparisons between experimental results and numerical simulations for configuration II as a function of the PS length

In Fig. 13, we compare the experimental results and numerical simulations for configuration II as a function of the length h of the PS. The FWHM of the output intensity profile in the Y-direction is depicted as a function of the incident average intensity for three different lengths h of the PS (see Fig. 1a-b in the main article).

One can see that, for the largest h equal to $500 \mu\text{m}$, the computed Y-axis FWHM of the beam at the output facet of the full structure are in fair agreement with the experimental results. Nevertheless, it must be pointed out that the profiles along Y-axis are no longer simple Gaussian or hyperbolic secant at high intensities. At high power regime, the profiles have multiple symmetric peaks as observed experimentally (Fig. 5 in the main article) and numerically (Fig. 6 in the main article). Consequently the FWHM is neither sufficient nor adequate to describe

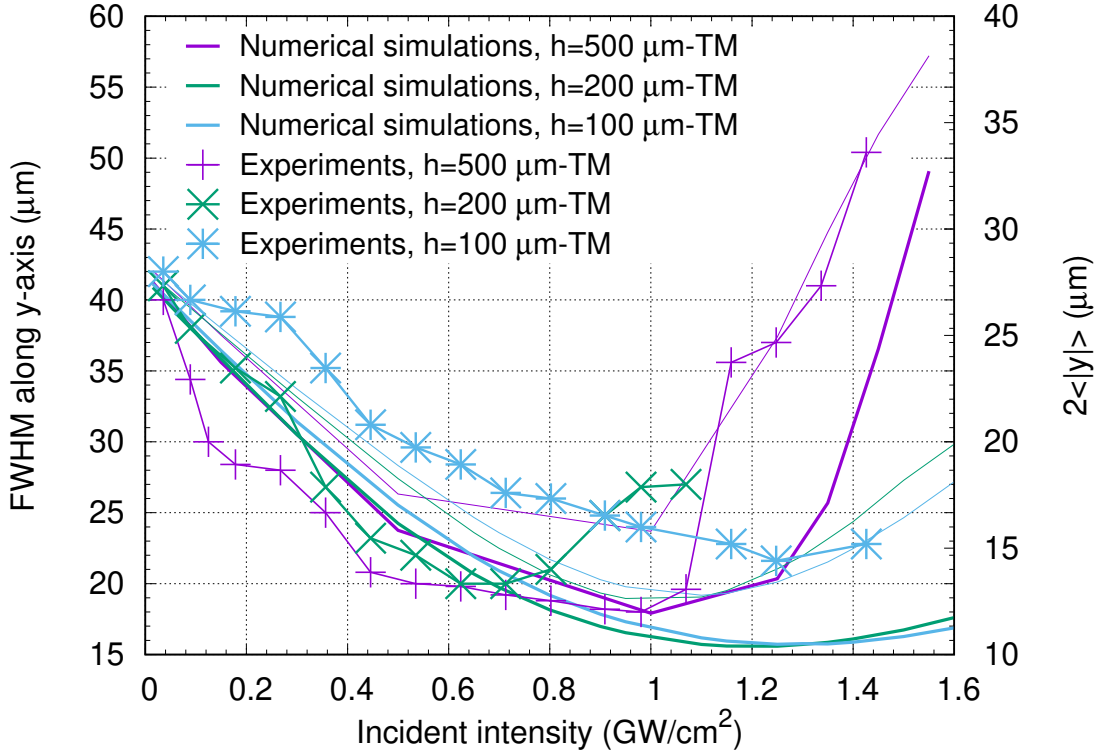


Figure 13: Computed and measured output beams FWHM along Y-axis for configuration II as a function of the input intensity for three different length h of the PS. On the right vertical scale, the corresponding computed mean full width $2 \langle |y| \rangle$ of the output beam along the Y-axis are given (see the text for its definition) using thin curves.

the features of the beam profile along the Y axis. The reported defocusing of the output beam observed experimentally for the highest intensity is also linked to the generation of these lateral peaks. This is seen above 1 GW/cm^2 for configuration II for $h = 500 \text{ } \mu\text{m}$ both in the experiments and in the simulations. Note that this defocusing effect was not seen in the FWHM experimental results in configuration I. The main reason is that the PS is located at the imaged output face of the full structure and consequently no diffraction can occur contrary to configuration II where the beam propagates some distance in the dielectric structure before its analysis. Nevertheless, when we increase the power of the input beam in the numerical simulations above 2 GW/cm^2 in configuration I for $h = 660 \text{ } \mu\text{m}$, the generation of small lateral peaks are observed similarly as for configuration II. We infer that in the experiments for configuration I, the intensity reaching the PS structure is too low to induce the lateral peaks, and consequently the broadening regime of beam is not yet reached.

For $h = 200 \text{ } \mu\text{m}$, one can see that the measured and simulated results are also in good agreement up to 0.8 GW/cm^2 . Above this intensity, the simulations cannot reproduce the increase of the FWHM followed by a short plateau (only two experimental points for this plateau). For $h = 100 \text{ } \mu\text{m}$, the experimental curve exhibits a gradual decrease followed by a

final stabilization of the measured FWHM of the output beam. As already mentioned at the beginning of section D.2 and as illustrated in Fig. 5 of the article, the beam profiles contain multiple lateral peaks when the incident intensity becomes large. When this regime starts the FWHM does not reflect it since the smaller lateral peaks do not modify the FWHM. Consequently, the discrepancies between the experimental results and the numerical simulations increase with the incident intensity, up to the intensity requested to generate the high lateral peaks.

To allow our simplified model to take into account at least qualitatively the impact of the multiple lateral peaks on the spatial spreading of the output beam widths along the Y -axis we compute the quantity $2 \langle |y| \rangle$ defined by:

$$2 \langle |y| \rangle \equiv 2 \int_{Y\text{-section}} |y| |E|^2(y, z_{out}) dy / \int_{Y\text{-section}} |E|^2(y, z_{out}) dy$$

where z_{out} is the z -coordinate of the output face of the full structure. This quantity $2 \langle |y| \rangle$ corresponds to the mean full width along the Y -axis of the symmetric profiles under investigation, it can capture the influence of the multiple lateral peaks even if their maximum values do not reach the half maximum of the central peak. The corresponding curves for the three structures we studied in configuration II ($h = 500, 200, 100 \mu\text{m}$) are the thin ones in Fig. 13 linked to the right vertical scale. As it can be seen, the results are in better agreement qualitatively with the experimental data than the direct output of the simulated FWHM. They show that the increase of the width of the output beam appears for smaller values of the incident intensities compared the results given by the simulations of the FWHM even if quantitatively the increase observed for $h=200 \mu\text{m}$ as a function of the incident intensity is not obtained from $0.7 \text{ GW}/\text{cm}^2$ but from $1.1 \text{ GW}/\text{cm}^2$.

E Complementary results for configurations I, II, and III

In Fig. 14, we provide the comparisons of the computed and measured Y -axis FWHM output beams for the three configurations I, II, III for the largest h value of each configuration as a function of the input beam intensity. As it can be seen, the computed FWHM curves follow partially the ones of the experimental data except for configuration III where the incident intensity of the PS segment is larger due to the shorter distance (1 mm) between the input facet of the structure and the PS compared to configuration II (4 mm) and configuration III (4.5 mm). For configuration III, the numerical results don't show any increase for the FWHM. Nevertheless, if we look at the results provided by mean full width $2 \langle |y| \rangle$ of the output beam, we see that we obtain a better qualitative agreement for the comparisons, for configurations I and II the simulation results stay globally correct while, for configuration III, we get the expected increase of the output beam width even if it appears for larger incident intensities compared to the experimental data.

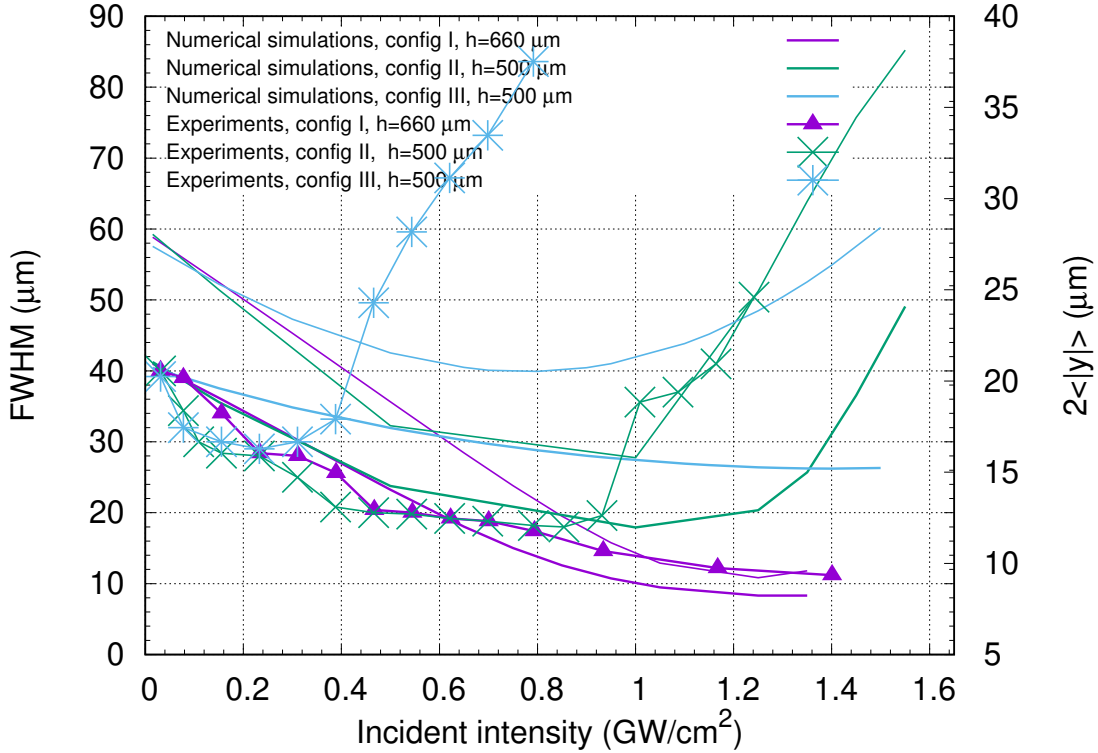


Figure 14: Computed and measured Y-axis FWHM output beams for the three configurations I, II, III as a function of the input beam intensity. On the right vertical scale, the corresponding computed mean full width $2 \langle |y| \rangle$ of the output beam along the Y-axis are given (see the text for its definition) using thin curves.

F Discussion on the limitations of the SNLSE

In this section, we extend the discussion summarized in the main article. It must be pointed out that the validity of our model does not extend to very high intensities. Indeed, in addition to the influence of higher order nonlinearities, the uncertainties on the considered nonlinear parameters (n_2 , α_2) may have a larger impact as one moves away from the linear regime. Furthermore, the hypothesis on the propagation model themselves are also becoming less and less valid as the incident intensity increases. A full treatment of the Kerr nonlinearity considering the Maxwell's equations [10, 11, 12] is more adequate than the Schrödinger equation. We must also remind that in the present form the solved SNLSE includes only one mode in the description of the nonlinear wave propagation as it is the case in the simple NLSE where the waveguide is usually assumed to be single-mode [4]. At high intensities this description may be no longer valid.

The limitations of the SNLSE can be at the origin of the observed discrepancies between the simulations results and the experimental ones. As an example, for configuration I and II, even if the numerical spatial profiles for the fields contain symmetric multipеaks like the recorded ones and have quite similar FWHM, they differ quantitatively: their lateral peak

positions being more distant to the beam center than the experimental ones for the same incident intensity. This phenomenon is similar to the predictions of 2D FDTD simulations of homogeneous Kerr media in which above some intensities the incident beam does not form a unique spatial soliton but a central peak with several lateral beams that diverge but with smaller angles than the ones seen in Fig. 6 (see appendix C in [13]). Nonlinear FDTD simulations, eventually 3D ones, are needed to investigate more precisely these differences. Ultimately, the full numerical study of the plasmon-soliton waves should be realized within a nonlinear 3D approach. A supplementary reason not mentioned above comes from the layered geometry of the investigated structure. In our 2D SNLSE model the impact of the layered structure is only taken into account through the opto-geometrical nonlinear factor η_x^{1D} , the weak variation of the propagation constants and the losses. The computational resources to realize such 3D simulations is huge due to the large sizes of the studied structures. For a homogeneous cartesian grid of $\lambda/10$ sampling at $\lambda = 1.55\mu\text{m}$ and considering only half of the structure thanks to the symmetry properties, the order of magnitude of cells is $5 \cdot 10^6$. This estimation is done without taken into account the grid size to correctly describe the nanoscale silica buffer and gold layers (10 grid cells to described the silica layer thickness means a 1 nm grid size, to be compared to the $0.155\mu\text{m}$ of the coarser grid). Consequently, such simulations cannot be realized efficiently realized without a non-uniform grid nonlinear 3D FDTD software. Furthermore, the above estimations do not consider the supplementary computational cost generated by the treatment of the nonlinearity in the FDTD code as it is explained in reference [14].

G Test of thermal effects

In order to test possible thermal effects on the focusing properties of the beam we have followed the procedure used in the litterature [15, 16]: to lower the time average power while maintaining the peak power an optical chopper was inserted on the beam path. In a previous work on spatial soliton in a chalcogenide waveguide of similar composition, we have already proven that the thermal effects is negligible both at 1550 nm and at 1200 nm using the same femtosecond laser [5]. In order to check this behavior for the present chalcogenide structure, we repeated the chopper experiment with a decrease by 40% of the time average intensity for the configuration III for $h = 500\mu\text{m}$. The results are given in Fig. 15. Within the experimental errors, there is no change in the measured FWHM as a function of the incident intensity. These results confirm that thermal effect can be neglected in all the studied configurations since the PS of configuration III receives the highest power due to its nearest position from the input facet.

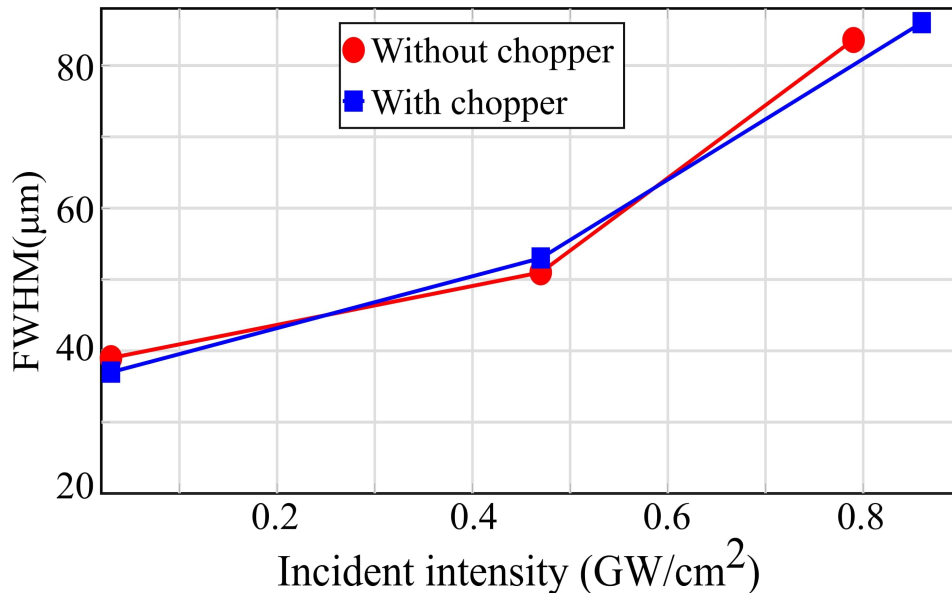


Figure 15: Evolution of the output beam FWHM as a function of incident intensity for configuration III with and without optical chopper.

References

- [1] M. M. R. Elsayy and G. Renversez. Exact calculation of the nonlinear characteristics of 2D isotropic and anisotropic waveguides. *Opt. Lett.*, 43(11):2446–2449, 2018.
- [2] Y. S. Kivshar and G. P. Agrawal. *Optical Solitons, From Fibers to Photonic Crystals*. Academic Press, 2003.
- [3] Peter E. Powers and Joseph W. Haus. *Fundamentals of Nonlinear Optics*. CRC Press, 2nd edition edition, 2017.
- [4] G. P. Agrawal. *Nonlinear fiber optics*. Academic Press, 3rd edition, 2001.
- [5] T. Kuriakose, E. Baudet, T. Halenkovič, M. M.R. Elsayy, P. Němec, V. Nazabal, G. Renversez, and M. Chauvet. Measurement of ultrafast optical kerr effect of ge-sb-se chalcogenide slab waveguides by the beam self-trapping technique. *Opt. Comm.*, 403:352 – 357, 2017.
- [6] Katsunari Okamoto. Chapter 5 - nonlinear optical effects in optical fibers. In Katsunari Okamoto, editor, *Fundamentals of Optical Waveguides (Second Edition)*, pages 209 – 259. Academic Press, second edition edition, 2006.
- [7] J. Hult. A Fourth-Order Runge-Kutta in the Interaction Picture Method for Simulating Supercontinuum Generation in Optical Fiber. *IEEE J. Lightwave Technol.*, 25(12):3770–3775, 2007.

- [8] J.Zweck O. V. Sinkin, R. Holzlohner and C. R. Menyuk. Optimization of the Split-Step Fourier Method in Modeling Optical Fiber Communications Systems. *IEEE J. Lightwave Technol.*, 21(1):61–68, 2003.
- [9] M. El-Amraoui, J. Fatome, J. C. Jules, B. Kibler, G. Gadret, C. Fortier, F. Smektala, I. Skripatchev, C.F. Polacchini, Y. Messaddeq, J. Troles, L. Brilland, M. Szpulak, and G. Renversez. Strong infrared spectral broadening in low-loss As-S chalcogenide suspended core microstructured optical fibers. *Opt. Express*, 18(5):4547–4556, 2010.
- [10] Nail Akhmediev, Adrian Ankiewicz, and Jose Maria Soto-Crespo. Does the nonlinear Schrödinger equation correctly describe beam propagation? *Opt. Lett.*, 18(6):411, 1993.
- [11] Y. Chen and J. Atai. Maxwell’s equations and the vector nonlinear Schrödinger equation. *Physical Review E*, 55:3652–3657, 1997.
- [12] F. Drouart, G .Renversez, A. Nicolet, and C. Geuzaine. Spatial Kerr solitons in optical fibers of finite size cross section: beyond the Townes soliton. *J. Opt. A: Pure Appl. Opt.*, 10:125101, 2008.
- [13] W. Walasik. *Plasmon–soliton waves in metal-nonlinear dielectric planar structures*. phdthesis, Aix-Marseille Université, 2014.
- [14] A. Taflove, A. Oskooi, and S. G. Johnson, editors. *Advances in FDTD Computational Electrodynamics*. Photonics and Nanotechnology. Artech House, Boston, 2013.
- [15] M. Falconieri and G. Salvetti. Simultaneous measurement of pure-optical and thermo-optical nonlinearities induced by high-repetition-rate, femtosecond laser pulses: application to cs₂. *Applied Physics B*, 69(2):133–136, Aug 1999.
- [16] Andrea Gnoli, Luca Razzari, and Marcofabio Righini. Z-scan measurements using high repetition rate lasers: how to manage thermal effects. *Opt. Express*, 13(20):7976–7981, Oct 2005.